Plasticity of a TiCu-based bulk metallic glass: Effect of cooling rate

J. Shen,[a)] Y.J. Huang, and J.F. Sun
School of Materials Science and Engineering, Harbin Institute of Technology, Harbin 150001, China

Compressive deformation was experimentally investigated for $Ti_{41.5}Cu_{42.5}Zr_{2.5}Hf_5Ni_{7.5}Si_1$ bulk metallic glass (BMG) fabricated at different cooling rates. It was found that the ductility of the BMG alloy increased with increasing of the cooling rate in solidification. The alloy with a monolithic amorphous structure exhibited a large ductility, up to 12%. The effect of cooling rate on the ductility of the BMG alloy is interpreted in terms of the variation in amorphous nature and free volume of the as-cast materials.

I. INTRODUCTION

As a class of advanced materials, bulk metallic glasses (BMGs) have gained considerable attention due to their unique properties, including high strength, corrosion resistance, wear resistance, and relatively low elastic modulus, etc., which are rarely found in crystalline materials.[1–3] The processing and widespread applications of BMGs are severely inhibited, however, by usually failing catastrophically on one dominant shear band and resulting in very limited macroscopic plastic strain (usually <2%) prior to failure at room temperature. To circumvent the drawback of limited plasticity of BMGs, recent attempts have focused on the preparation of BMG matrix composites.[4–10] BMG matrix composites can be achieved by in-situ formation of ductile crystalline phase in the amorphous matrix from the melt during casting,[4,5] by partial crystallization of the as-cast BMGs,[6] or by addition of reinforcing materials using casting or powder warm processing method.[7–9] The ultimate aim of these attempts is to block the rapid propagation of shear bands, leading to multiplication, branching, and restriction of shear bands, which in turn allows for promoted global ductility of the materials.

Very recently, it has been reported that some so-called "ductile" BMGs, such as $Zr_{59}Ta_5Cu_{18}Ni_8Al_{10}$,[11] $Pt_{57.5}Cu_{14.7}Ni_{5.3}P_{22.5}$,[12] $Cu_{47.5}Zr_{47.5}Al_5$,[13–15] and $Cu_{43}Zr_{43}Al_7Ag_7$ BMGs,[16,17] exhibit large plastic strain (5–20%) before failure.[11–30] Multiplication, intersection, and branching of shear bands were observed on the surfaces of the fractured samples for these ductile BMGs. Up to now, although the enhanced ductility of BMGs has

been attributed to these shear band features, the intrinsic reasons continue to pose significant fundamental challenges. The observed large ductility of the selected BMG alloys are often explained in terms of (i) the precipitation of nanocrystallites in the metallic glassy matrix[18,19]; (ii) crystallization-induced plasticity[20–22]; (iii) 1–2 nm scale medium-range ordering[11,23–26]; (iv) phase separation into regions of different compositions[17]; (v) high Poisson ratio[12,27]; and (vi) addition of an alloying element with a positive heat of mixing with the other constituting elements.[28,29]

Lin and Johnson[31] developed TiCu-based BMGs with high glass-forming ability in the quaternary Ti–Cu–Ni–Zr alloy system. In particular, this class of low-cost BMGs exhibits interesting mechanical properties and triggers attention from researchers.[18,29,31,32] Ma et al.[32] have attempted to increase the titanium content and succeeded in synthesizing a TiCu-based BMG with nearly equal amounts of Cu and Ti atoms, i.e., $Ti_{41.5}Cu_{42.5}Zr_{2.5}Hf_5Ni_{7.5}Si_1$.

In this paper, the compressive deformation characteristics of $Ti_{41.5}Cu_{42.5}Zr_{2.5}Hf_5Ni_{7.5}Si_1$ BMG are investigated. The $Ti_{41.5}Cu_{42.5}Zr_{2.5}Hf_5Ni_{7.5}Si_1$ alloy possesses high fracture strength above 2190 MPa and has a large plastic strain up to 12% in compression tests at room temperature. It is found that the alloy shows varying levels of ductility, strongly depending on its cooling rates during solidification.

II. EXPERIMENTAL PROCEDURES

Alloy ingots with nominal composition of $Ti_{41.5}Cu_{42.5}Zr_{2.5}Hf_5Ni_{7.5}Si_1$ (at.%) were prepared by arc melting a mixture of pure elements with purities >99.9% in a titanium-gettered high-purity argon atmosphere. The alloy ingots of the desired composition were remelted at

---
[a)]Address all correspondence to this author.
   e-mail: junshen@hit.edu.cn

least three times to obtain a high chemical homogeneity. Rodlike amorphous samples were prepared by drop casting the melts into a copper mold, and the obtained samples have a steplike outward appearance, as illustrated in Fig. 1. The microstructure of the as-cast samples was characterized by transmission electron microscopy (TEM). TEM specimens were mechanically thinned and polished to be <10 μm thick. The ground specimens were supported by a Mo mesh and then subjected to ion milling at an incident angle of 5° for <30 min to electron transparency by using a Gatan (Pleasanton, CA) 691 precision ion polishing system with liquid nitrogen cooling. TEM observations were conducted on JEOL JEL-2010 (JEOL, Tokyo, Japan) and Philips CM 200/FEG (FEI, The Netherlands) machines operating at 200 kV. To determine the thermal properties of the alloys, thermal analysis was performed using differential scanning calorimetry (DSC) at a constant heating rate of 20 K/min in a flow of purified argon gas. From the as-cast rods, the cylindrical samples for the compression tests were prepared with an aspect ratio of 2:1, and both ends of the samples were polished to make them parallel to each other. The room-temperature compression tests were conducted on an Instron 5500 (Norwood, MA) mechanical instrument under an initial strain rate of 4×10^{-4} s^{-1}. The compression test samples were taken from selected locations along the longitudinal direction of the cast rods, as shown in Fig. 1, where the sample III represents the location of the top end of the copper mold, sample I is close to the low end of the copper mold, and the sample II is between them. Due to the differences in the distance from the top end of the copper mold and the section diameter of the samples, it can be reasonably judged that the cooling rates for the three samples for compression tests are gradually increased from sample III to sample I, i.e., sample I has the highest cooling rate among the three samples. After compression tests, the fracture surfaces of the samples were observed by scanning electron microscopy (SEM).

III. RESULTS

Figure 2 shows the nominal stress–strain curves of the samples. All these samples show linear elasticity up to a strain of ~2.4% and a high maximum compressive strength >2190 MPa prior to failure, but they exhibit
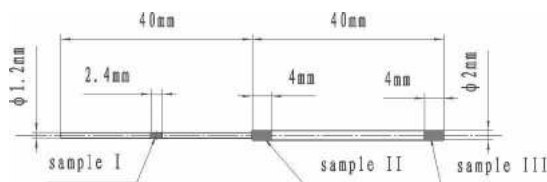

FIG. 1. Sketch showing the geometry of the as-cast BMG bar and locations of the samples used for compression tests, TEM, and thermal analysis.
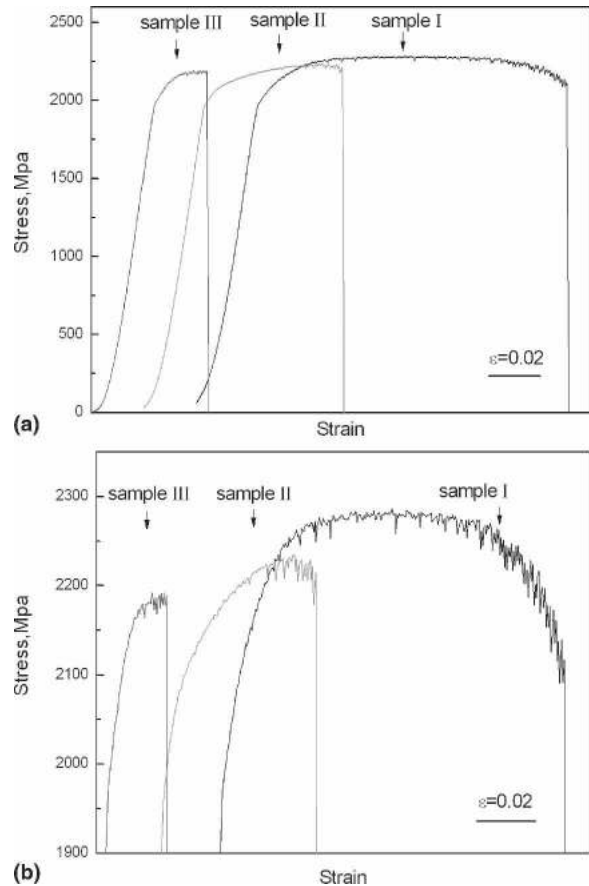

FIG. 2. Compressive stress–strain curves for the three BMG samples: (a) complete curves and (b) enlarged curves showing detailed serrated patterns.

different degrees of plasticity. The mechanical properties of the three samples are summarized in Table I. The compressive plasticity follows an increasing order of sample III, sample II, and sample I. The compression test data are confirmed being reproducible by conducting two or three separate measurements for the respective cast samples and obtaining essentially similar results. Detailed observation of the stress–strain curves of the three samples shows that serrated flow is apparent in the plastic regions of the stress–strain curves after yielding. Figure 2(b) shows enlarged portions of the stress–strain curves for the samples highlighting the details of the

TABLE I. Yield strength (σ_y), maximum compressive strenth (σ_m), elastic strain (ϵ_e), plastic strain (ϵ_p), compressive total strain to failure (ϵ_f), compressive shear fracture angle θ_c^F, and primary shear band angle θ_c^0 for the three studied samples of Ti$_{41.5}$Cu$_{42.5}$Zr$_{2.5}$Hf$_5$Ni$_{7.5}$Si$_1$ alloy exhibiting different plasticities before failure.

Sample	σ_y (MPa)	σ_m (MPa)	ϵ_e (%)	ϵ_p (%)	ϵ_f (%)	θ_c^F (°)	θ_c^0 (°)
I	1945	2285	2.3	12	14.3	45	41.6
II	1954	2232	2.3	7.3	9.6	43	41
III	1979	2190	2.4	2.1	4.5	40.5	40

serration features. For sample III, the number of serration steps in the stress–strain curve is relatively small, and sample I shows the most serration steps among the three samples. Because it has been widely accepted that the stress drop for each serration on a stress–strain curve corresponds to the nucleation of a single shear band, in some extent, the number of serrations on the stress–strain curve can reflect the plastic deformation ability of the materials.

Figure 3 presents the SEM images showing the side-view appearances of the fractured samples. Evidently all of the samples exhibit a perfect shear fracture characterized by well-defined fracture angles (between the fracture plane and the loading axis), which are, respectively, 45°, 43°, and 40.5° for sample I, sample II, and sample III. It is interesting to note that the fracture angles are all close to 45°, typical for most of BMG alloys,[33,34] but increase with increasing of the compressive ductility of the samples. Figure 4 displays the SEM images of the external surfaces of the samples near the fractured regions. Shear bands are easily visible on all three samples' surfaces. Primary shear bands are formed along a direction nearly parallel to that of the shear plane, i.e., roughly 40–45° with respect to the direction of loading axis, as marked by black arrows in the figures, and some secondary shear bands appear at an angle of 40–60° from primary shear bands, as marked by white arrows in the figures. However, the number of visible shear bands at a particular magnification decreases in the order of sample I, sample II, and sample III. For sample III, the shear bands are, to a great extent, straight and usually exist as well-separated steps [see Fig. 4(c)]. In contrast, for sample II, most of the shear bands are jagged and unevenly distributed near the fracture region. The secondary shear bands with spacing of 10–20 μm can be easily found [see Fig. 4(b)]. For sample I, the shear bands are highly branched, as depicted in Fig. 4(a). The interspac-

ing distance of secondary shear bands of the sample I is about 2–5 μm, indicating the formation of a high density of shear bands. As is well known, the plastic deformation achieved by BMGs is usually accommodated through the generation of multiple shear bands; the degree of plastic deformation in BMGs is largely dependent on the densities of shear bands generated during deformation.[22] Following the order of sample III, sample II, and sample I, the external surfaces of the deformed samples generate more and more shear bands, thus revealing increasing plastic deformation ability, which is consistent with the results shown in Fig. 1 and Table I.

Figure 5 shows the fracture surfaces of the three samples. It can be seen that the fracture surfaces are covered mostly with riverlike patterns which consist of main streams, tributaries, and intermittent smooth regions, as shown in Figs. 5(a), 5(c), and 5(e). For sample I, the river lines are dense and heavily entangled [Fig. 5(a)], which is a good phenomenological indicator of inherent plasticity. In contrast, the main streams of the river-like patterns for samples II and III are becoming straight [Figs. 5(c) and 5(e)], indicating an increasing brittleness extent of the glassy material. Examination of the fracture surfaces at high magnification reveals well-developed vein patterns [Figs. 5(b), 5(d), and 5(f)], typical of fracture of a metallic glass.[35] It is evident that, as compared to samples II and III, the vein patterns for sample I are high in density, small in size, and exhibit a distinct trace of viscous flow, suggesting the capability of undergoing extensive plastic deformation prior to failure.

Because the mechanisms governing plastic deformation of BMGs are closely linked to their structure, the microstructures of the three samples are subsequently examined by TEM. Figure 6 shows the bright-field TEM image obtained from as-cast sample III. Evidently, over a wide area, the structure of the sample is
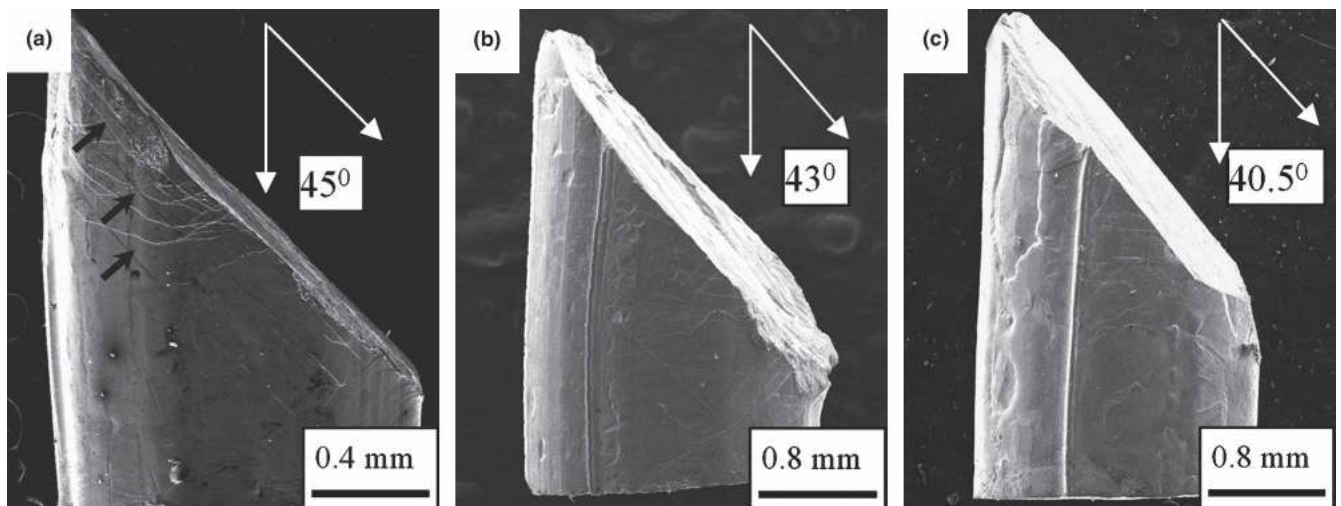

FIG. 3. SEM images showing the side-view appearances of the fractured samples: (a) sample I, (b) sample II, and (c) sample III.
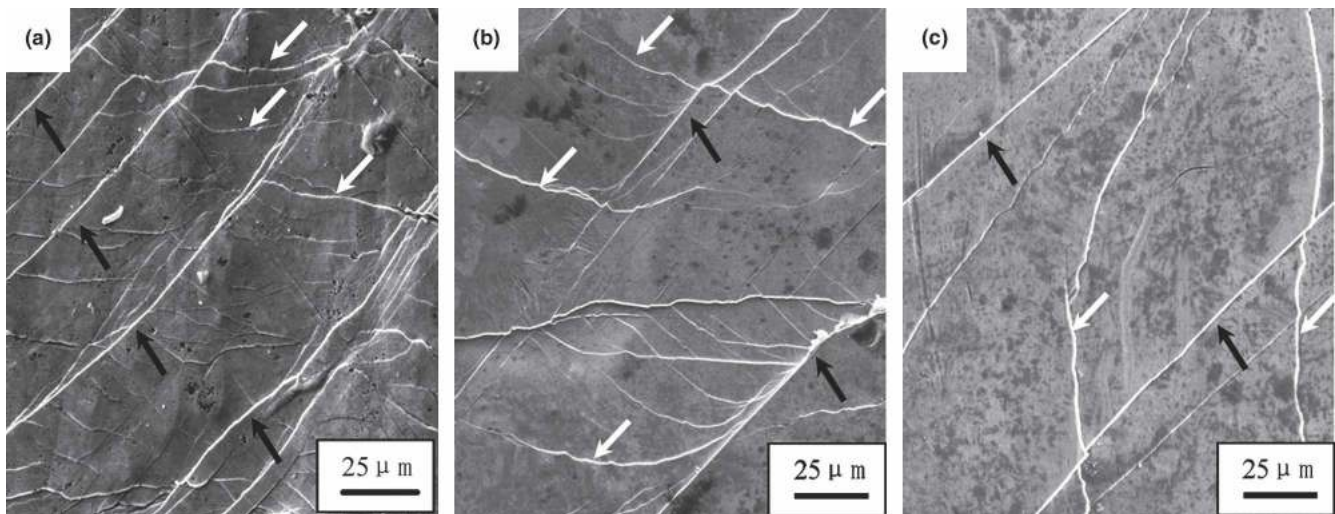
FIG. 4. SEM images showing the external surfaces of the fractured samples near the fractured regions for the samples: (a) sample I, (b) sample II, and (c) sample III.

wholly featureless (ignoring the contrast due to the curly edges of the holes in the TEM specimen), representing a fully amorphous structure without any trace of crystallites. The solely amorphous phase can be confirmed by the smooth diffuse ring on the corresponding selected area electron diffraction pattern (inset of Fig. 6). The TEM images for samples I and II give a quite similar contrast (not shown), implying that all of the samples are nearly amorphous. Nevertheless, only the high-resolution TEM image of sample I shows a perfectly amorphous structure on the atomic scale, as shown in Fig. 7(a). In contrast, there are a few nano-sized crystals embedded in the amorphous matrix of the samples II and III, as circled in Figs. 7(b) and 7(c). In addition, the nanocrystals in sample II are obviously smaller both in size and in population than those of sample III. It can be seen that the fully amorphous structure guarantees the high plasticity for the sample I; and as the nanocrystals in the as-cast samples are larger in size or in density, the plasticity of the alloy will be smaller.

Figure 8 shows the DSC curves for the three studied samples at a constant heating rate of 20 K/min. All the three samples exhibit an endothermic event, characteristic of the glass transition, followed by at least three exothermic peaks due to a multistage crystallization. The glass transition temperatures (T_g) and the onset temperatures of crystallization (T_x) for the three samples are almost same within the experiment error, indicating the comparable thermal stability of the samples with the same composition. However, careful calculation of the crystallization enthalpies from the DSC curves by integrating the areas corresponding to the crystallization peaks indicate that sample III has the smallest enthalpy of crystallization, reflecting the largest amount of crystallites contained in the as-cast state due to an insufficient

cooling rate during solidification, as compared to other samples. The calculated enthalpies of crystallization for the samples are given in Table II.

IV. DISCUSSION

Since the discovery of BMGs, continuous attempts have been made to understand and explore the macroscopic ductility of this class of new materials through fine tuning the compositions or tailoring the microstructure of alloys. Very recently, a significant ductility has been observed in glassy alloys based on Cu,[18,20,29] Zr,[11,19,21] Pt,[12] Ni,[25,28] Ti,[23,24,30] Pd,[27] and CuZr.[13–17,22,26] In this paper, we have demonstrated that the ductility of the TiCu-based metallic glass strongly depends on the cooling rates in solidification and thus on its structure. The change of ductility of the BMG with cooling rates/structure can be manifested by the fracture characteristics. For the samples with the same composition but different cooling rates, their fracture surfaces show typical veinlike patterns with varying levels of development. More interestingly, the fracture angles vary with the ductilities of the samples, implying an underlying deformation mechanism mightily correlated with their structure. Zhang et al.[33] suggested that the final shear fracture of some nanostructured composites could be explained by a rotation mechanism of the shear bands induced by the high compressive plasticity. In this study, the plastic strain observed for sample I, sample II, and sample III is 12%, 7.3%, and 2.1%, respectively. Therefore, the rotation mechanism of the shear bands can also be applied to the present ductile TiCu-base alloy. Based on that the volume of the sample and the length of the primary shear band remain nearly
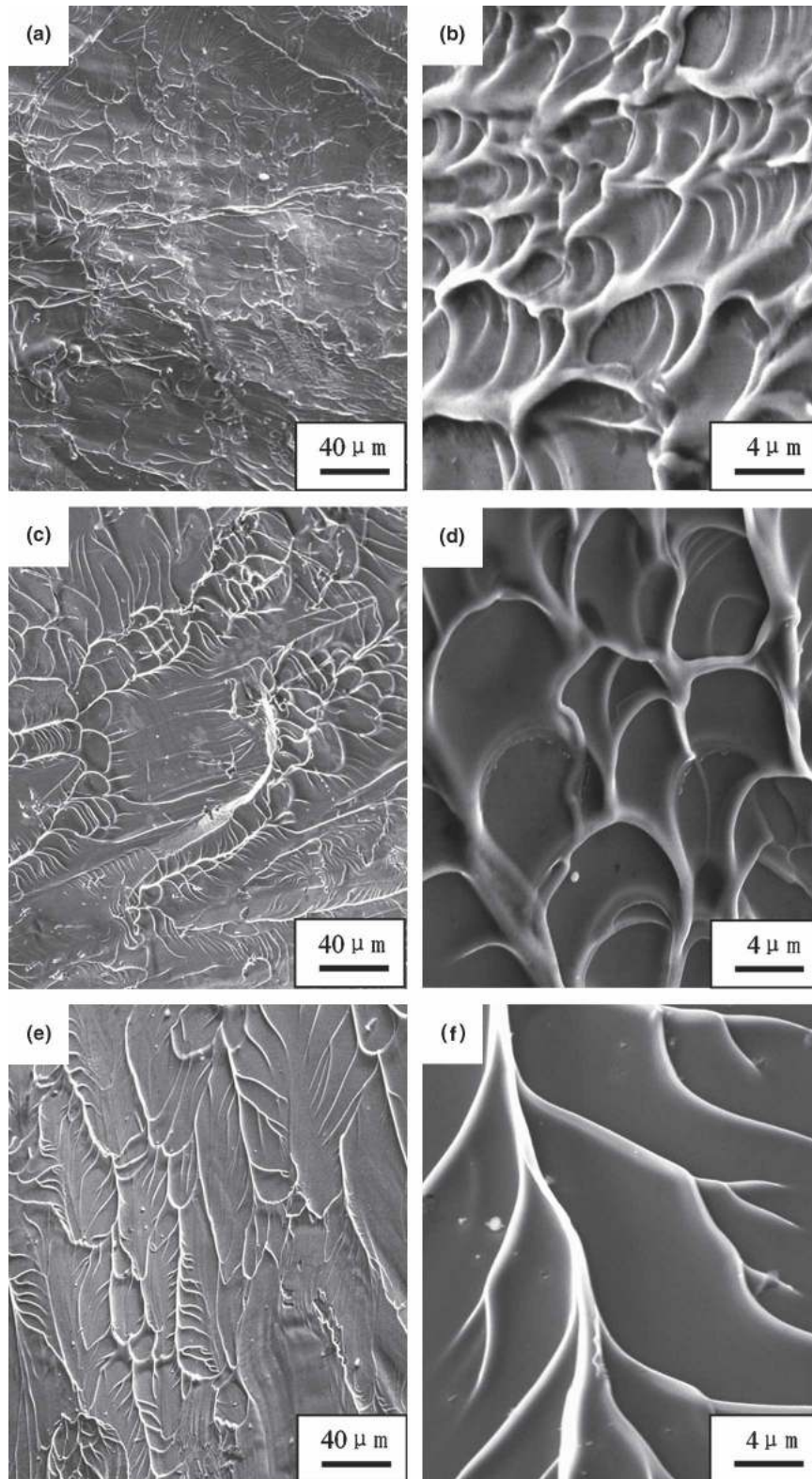
FIG. 5. SEM images showing the fracture surfaces of the samples: (a, b) sample I, (c, d) sample II, and (e, f) sample III.

constant before and after deformation, the relationship among the primary shear band angle θ_c^0, the compressive shear fracture angle θ_c^F, and the plastic strain ϵ_p can be established as[33]

$$\sin(\theta_c^0) = \sqrt{1 - \epsilon_p} \, \sin(\theta_c^F) \quad . \qquad (1)$$

Consequently, the primary shear band angle θ_c^0 can be approximately calculated if the compressive plastic strain
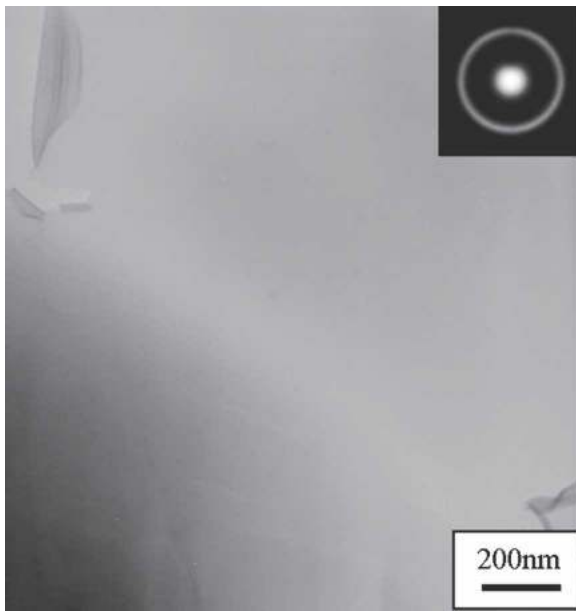
FIG. 6. Bright-field TEM image and the corresponding selected area electron diffraction (inset) of sample III.

FIG. 8. DSC curves for the three studied samples of $Ti_{41.5}Cu_{42.5}Zr_{2.5}$ $Hf_5Ni_{7.5}Si_1$ alloy at a constant heating rate of 20 K/min.

ϵ_p and the compressive shear fracture angle θ_c^F are known from this relationship. By substituting the values of ϵ_p and θ_c^F into Eq. (1), the primary shear band angles θ_c^0 for sample I, sample II, and sample III are calculated to be 41.6°, 41°, and 40°, respectively. Hence, the primary shear band angles θ_c^0 for the three samples with respect to the stress axis are in the range 40–42°. This result agrees well with the previous observations for other BMGs and nanostructured composites and indicates that the deformation of the BMG alloy of this study satisfies the Mohr–Coulomb criterion.[15,33,34]

It is now well established that an excess amount of free volume is frozen into the atomic scale structure due to the nonequilibrium processing conditions during cooling of a
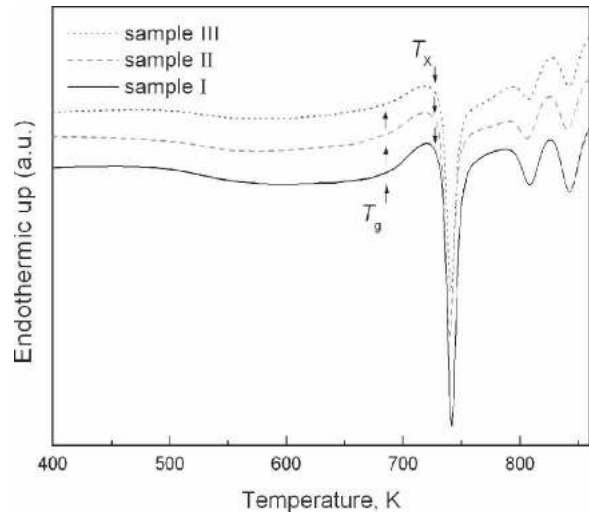
TABLE II. Thermal properties of the three samples; ΔH_0 denotes the structural relaxation exothermic heat, and ΔH_1, ΔH_2, and ΔH_3 denote the exothermic heats of the first, second, and third stages of crystallization, respectively.

Sample	ΔH_0 (J/g)	ΔH_1 (J/g)	ΔH_2 (J/g)	ΔH_3 (J/g)	$\sum \Delta H = \Delta H_1 + \Delta H_2 + \Delta H_3$ (J/g)
I	−4.6	−7.1	−1.7	−2.6	−11.40
II	−4.4	−5.5	−1.65	−2.0	−9.15
III	−3.7	−5.2	−1.4	−1.8	−8.40

glass-forming material from the liquid state.[36] Free volume is generally defined as an excess volume relative to some reference state such as the hypothetical equilibrium liquid state. According to the free volume theory, the free volume of an atom is that part of its nearest neighbor cage in which the atom can move around and perform a
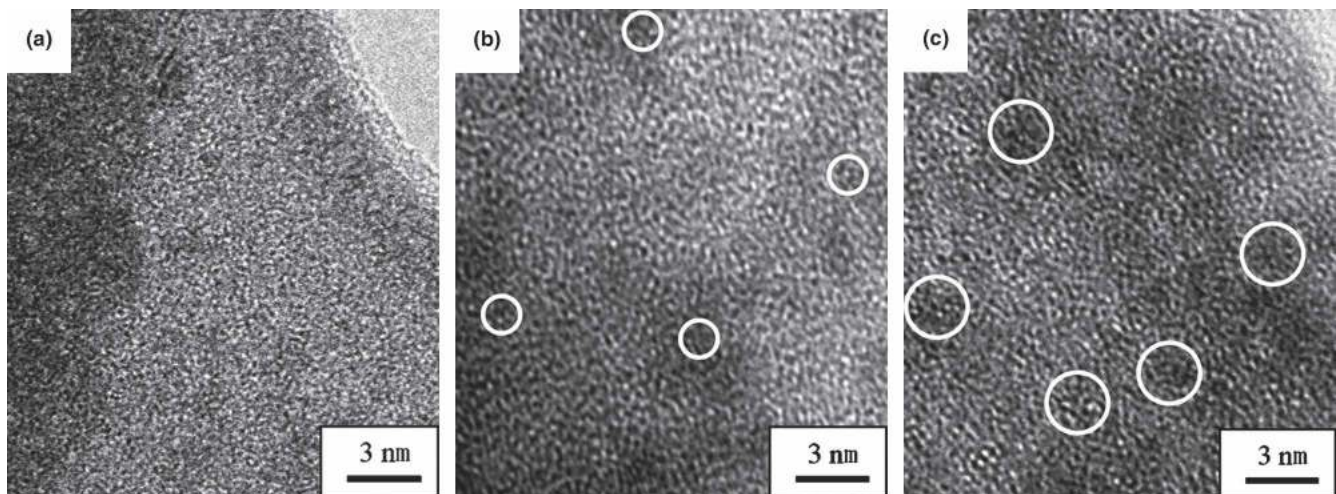

FIG. 7. High-resolution TEM images of as-cast samples: (a) sample I, (b) sample II, and (c) sample III.

diffusive or shear flow jump without any expenditure of energy. The amount of quenched-in free volume plays a very important role in plastic deformation of glassy alloys. Existing models for deformation of metal glasses predict that a reduction in free volume will inhibit plastic deformation.[37,38] Beukel et al.[39] have found that the free volume theory describes well the results of DSC measurements of metallic glasses and demonstrated that the amount of free volume in a metallic glass is proportional to the enthalpy released during structural relaxation. Figure 9 presents the enlarged sections of the DSC curves (Fig. 8) below the glass transition temperatures. The heat release events due to structural relaxation can be clearly seen from Fig. 9; and the enthalpies of relaxation can be calculated to be −4.6, −4.4, and −3.7 J/g for samples I, II, and III, respectively (see Table II). One can see that the change of enthalpies of relaxation follows a decreasing order of sample I, sample II, and sample III, i.e., the higher the cooling rate, the greater the enthalpy of relaxation, and thus the larger the amount of free volume in the amorphous sample. This trend suggests an obvious free volume mechanism controlling the ductility of the BMG alloy of this study.

Several different potential mechanisms for the improvement of the macroscopic ductility of BMGs have been proposed.[11–30] Schroers et al.[12] correlated the ductility of quaternary Pt–Cu–Ni–P BMGs with their high Poisson's ratio, which causes the tip of a shear band to extend rather than to initiate a crack. Oh et al.[17] suggested that the phase separation in the as-cast $Cu_{43}Zr_{43}Al_7Ag_7$ BMGs may be responsible for its high plastic strain. Park et al.[29] considered that addition of an alloying element with a positive heat of mixing with the other constituting elements, i.e., Ag in Cu–Zr–Al, Nb in Ni–Zr–Ti–Si–Sn, and Ta in Zr–Cu–Ni–Al, may provide atomic-scale local inhomogeneity, thereby enhancing the plasticity of BMGs. Zeng et al.[25] and Kim et al.[23] indicated that the existence of 1- to 2-nm-scale medium-range ordering embedded in the amorphous matrix may be effective to enhance the ductility of the BMGs. Calin et al.[18] explained the distinct global plasticity by a unique composite microstructure consisting of nanoscale crystals dispersed in the glassy matrix. Saida et al.,[21] Lee et al.,[22] and Men et al.[20] argued that nanocrystalline particles induced by deformation in the amorphous matrix can impede the propagation of shear bands, leading to enhanced plasticity. Our observations of this study, however, conflict with all of these mechanisms. On the one hand, instead of a mixture of amorphous matrix and nanocrystals, the single amorphous phase contributes the ductility of the TiCu-based BMG alloy, as shown in the case of sample I. As the cooling rate decreases, the samples contain more and larger nanocrystals, and thus the ductility becomes smaller, as seen in the cases of samples II and III. On the other hand, massive free volume trapped in the fast-cooled sample I enhances the plasticity of the studied BMG. As the cooling rate decreases, the amount of free volume in the samples II and III decreases, leading to reduced ductility. The large amount free volume makes the BMG (e.g., sample I) more shearable in deformation and therefore more ductile in compression. The ease of shearing of sample I can be reflected from the more distinctive serration in its stress–strain curve [Fig. 2(b)] and the larger number of shear bands on the external surface of the fractured specimen [Fig. 4(a)], as compared with samples II and III. On all accounts, fully amorphous structure and high concentration of free volume play a dominant role in the ductile deformation process of the amorphous alloys. A single amorphous structure and excessive free volume ensure a high plasticity, as encountered in sample I. This mechanism can explain why the amorphous ribbon samples can be ductile in bending while the bulk counterparts are often brittle upon any stress loading without appreciable ductility.
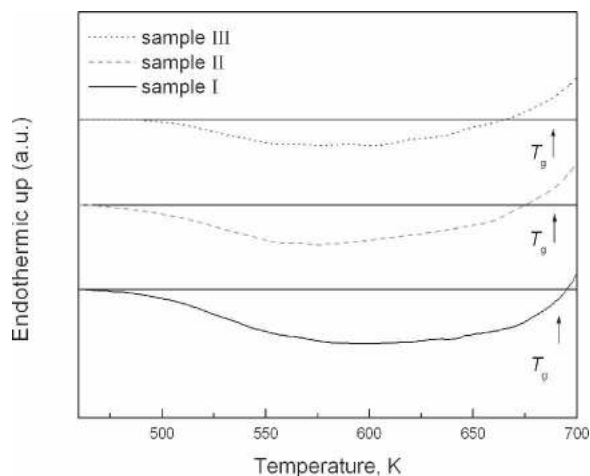
V. CONCLUSIONS

(1) The $Ti_{41.5}Cu_{42.5}Zr_{2.5}Hf_5Ni_{7.5}Si_1$ BMG alloy exhibits a large compressive ductility, and the ductile strain ability is strongly dependent on its cooling rate and thus on its as-cast structure. A single amorphous phase can significantly promote the plasticity of the BMG alloy.

(2) The large concentration of free volume trapped in the amorphous alloy with a high cooling rate in solidification is also evidently responsible for the enhanced ductility.

(3) The atomic-scale structure (amorphous nature and free volume concentration) and properties of BMGs are very sensitive to their thermal history. Caution should be exercised when we evaluate the ductility of a specific glass-forming alloy. Different portions of the amorphous

FIG. 9. Enlarged DSC curves (Fig. 8) below glass transition temperatures for the three studied samples.

alloy with the same composition could have largely different levels of ductility due to the different cooling rates.

REFERENCES

1. A. Inoue: Stabilization of metallic supercooled liquid and bulk amorphous alloys. *Acta Mater.* **48,** 279 (2000).
2. W.L. Johnson: Bulk glass-forming metallic alloys: Science and technology. *MRS Bull.* **24,** 42 (1999).
3. W.H. Wang, C. Dong, and C.H. Shek: Bulk metallic glasses. *Mater. Sci. Eng., R* **44,** 45 (2004).
4. G. He, J. Eckert, and W. Löser: Novel Ti-base nanostructure–dendrite composite with enhanced plasticity. *Nat. Mater.* **2,** 33 (2003).
5. C.C. Hays, C.P. Kim, and W.L. Johnson: Microstructure controlled shear band pattern formation and enhanced plasticity of bulk metallic glasses containing in situ formed ductile phase dendrite dispersions. *Phys. Rev. Lett.* **84,** 2901 (2000).
6. A. Inoue, T. Zhang, M.W. Chen, T. Sakurai, J. Saida, and M. Matsushita: Formation and properties of Zr-based bulk quasicrystalline alloys with high strength and good ductility. *J. Mater. Res.* **15,** 2195 (2000).
7. R.D. Conner, R.B. Dandliker, and W.L. Johnson: Mechanical properties of tungsten and steel fiber reinforced $Zr_{41.25}Ti_{13.75}Cu_{12.5}Ni_{10}Be_{22.5}$ metallic glass matrix composites. *Acta Mater.* **46,** 6089 (1998).
8. Y.C. Kim, E. Fleury, J-C. Lee, and D.H. Kim: Origin of the simultaneous improvement of strength and plasticity in Ti-based bulk metallic glass matrix composites. *J. Mater. Res.* **20,** 2474 (2005).
9. D.H. Bae, M.H. Lee, D.H. Kim, and D.J. Sordelet: Plasticity in $Ni_{59}Zr_{20}Ti_{16}Si_2Sn_3$ metallic glass matrix composites containing brass-fibers synthesized by warm extrusion of powders. *Appl. Phys. Lett.* **83,** 2312 (2003).
10. H. Choi-Yim and W.L. Johnson: Bulk metallic glass matrix composites. *Appl. Phys. Lett.* **71,** 3808 (1997).
11. L.Q. Xing, Y. Li, K.T. Ramesh, J. Li, and T.C. Hufnagel: Enhanced plastic strain in Zr-based bulk amorphous alloys. *Phys. Rev. B* **64,** 180201 (2001).
12. J. Schroers and W.L. Johnson: Ductile bulk metallic glass. *Phys. Rev. Lett.* **93,** 255506 (2004).
13. J. Das, M.B. Tang, K.B. Kim, R. Theissmann, F. Baier, W.H. Wang, and J. Eckert: "Work-hardenable" ductile bulk metallic glass. *Phys. Rev. Lett.* **94,** 205501 (2005).
14. K.B. Kim, J. Das, F. Baier, M.B. Tang, W.H. Wang, and J. Eckert: Heterogeneity of a $Cu_{47.5}Zr_{47.5}Al_5$ bulk metallic glass. *Appl. Phys. Lett.* **88,** 051911 (2006).
15. J. Eckert, J. Das, K.B. Kim, F. Baier, M.B. Tang, W.H. Wang, and Z.F. Zhang: High strength ductile Cu-base metallic glass. *Intermetallics* **14,** 876 (2006).
16. D.S. Sung, O.J. Kwon, E. Fleury, K.B. Kim, J.C. Lee, D.H. Kim, and Y.C. Kim: Enhancement of the glass forming ability of Cu-Zr-Al alloys by Ag addition. *Metal Mater. Int.* **10,** 575 (2004).
17. J.C. Oh, T. Ohkubo, Y.C. Kim, E. Fleury, and K. Hono: Phase separation in $Cu_{43}Zr_{43}Al_7Ag_7$ bulk metallic glass. *Scripta Mater.* **53,** 165 (2005).
18. M. Calin, J. Eckert, and L. Schultz: Improved mechanical behavior of Cu–Ti-based bulk metallic glass by in situ formation of nanoscale precipitates. *Scripta Mater.* **48,** 653 (2003).
19. W.B. Dong, H.F. Zhang, J. Cai, W.S. Sun, A.M. Wang, H. Li, and Z.Q. Hu: Enhanced plasticity in a Zr-based bulk metallic glass containing nanocrystalline precipitates. *J. Alloys Comp.* **425,** L1 (2006).
20. H. Men and T. Zhang: A bulk glassy Cu–Zr–Ti–Sn alloy with superior plasticity. *Mater. Trans.* **46,** 2545 (2006).
21. J. Saida, A.D.H. Setyawan, H. Kato, and A. Inoue: Nanoscale multistep shear band formation by deformation-induced nanocrystallization in Zr–Al–Ni–Pd bulk metallic glass. *Appl. Phys. Lett.* **87,** 151907 (2005).
22. S.K. Lee, M.Y. Huh, E. Fleury, and J.C. Lee: Crystallization-induced plasticity of Cu-Zr containing bulk amorphous alloys. *Acta Mater.* **54,** 349 (2006).
23. Y.C. Kim, J.H. Na, J.M. Park, D.H. Kim, Y.H. Lee, and W.T. Kim: Role of nanometer-scale quasicrystals in improving the mechanical behavior of Ti-based bulk metallic glasses. *Appl. Phys. Lett.* **83,** 3093 (2003).
24. J.M. Park, H.J. Chang, K.H. Han, W.T. Kim, and D.H. Kim: Enhancement of plasticity in Ti-rich Ti–Zr–Be–Cu–Ni bulk metallic glasses. *Scripta Mater.* **53,** 1 (2005).
25. Y.Q. Zeng, N. Nishiyama, T. Wada, D.V. Louzguine-Luzgin, and A. Inoue: Ni-rich Ni–Pd–P glassy alloy with high strength and good ductility. *Mater. Trans.* **47,** 175 (2006).
26. Z.W. Zhu, H.F. Zhang, W.S. Sun, B.Z. Ding, and Z.Q. Hu: Processing of bulk metallic glasses with high strength and large compressive plasticity in $Cu_{50}Zr_{50}$. *Scripta Mater.* **54,** 1145 (2006).
27. K.F. Yao, F. Ruan, Y.Q. Yang, and N. Chen: Superductile bulk metallic glass. *Appl. Phys. Lett.* **88,** 122106 (2006).
28. M.H. Lee, J.Y. Lee, D.H. Bae, W.T. Kim, D.J. Sordelet, and D.H. Kim: A development of Ni-based alloys with enhanced plasticity. *Intermetallics* **12,** 1133 (2004).
29. E.S. Park, D.H. Kim, T. Ohkubo, and K. Hono: Enhancement of glass forming ability and plasticity by addition of Nb in Cu–Ti–Zr–Ni–Si bulk metallic glasses. *J. Non-Cryst. Solids* **351,** 1232 (2005).
30. F.Q. Guo, H.J. Wang, S.J. Poon, and G.J. Shiflet: Ductile titanium-based glassy alloy ingots. *Appl. Phys. Lett.* **86,** 091907 (2005).
31. X.H. Lin and W.L. Johnson: Formation of Ti–Zr–Cu–Ni bulk metallic glass. *J. Appl. Phys.* **78,** 6514 (1995).
32. C.L. Ma, H. Soejima, S. Ishihara, K. Amiya, N. Nishiyama, and A. Inoue: New Ti-based bulk glassy alloys with high glass-forming ability and superior mechanical properties. *Mater. Trans.* **45,** 3223 (2004).
33. Z.F. Zhang, G. He, H. Zhang, and J. Eckert: Rotation mechanism of shear fracture induced by high plasticity in Ti-based nanostructured composites containing ductile dendrites. *Scripta Mater.* **52,** 945 (2005).
34. Z.F. Zhang and J. Eckert: Unified tensile fracture criterion. *Phys. Rev. Lett.* **94,** 094301 (2005).
35. C.T. Liu, L. Heatherly, D.S. Eaton, C.A. Carmichael, J.H. Schneibel, C.H. Chen, J.L. Wright, M.H. Yoo, J.A. Horton, and A. Inoue: Test environments and mechanical properties of Zr-base bulk amorphous alloys. *Metall. Mater. Trans. A* **29,** 1811 (1998).
36. D. Turnbull and M.H. Cohen: On the free-volume model of the liquid-glass transition. *J. Chem. Phys.* **52,** 3038 (1970).
37. P.S. Steif, F. Spaepen, and J.W. Hutchinson: Strain localization in amorphous metals. *Acta Metall.* **30,** 447 (1982).
38. F. Spaepen: A microscopic mechanism for steady state inhomogeneous flow in metallic glasses. *Acta Metall.* **25,** 407 (1977).
39. A. van den Beukel and J. Sietsma: The glass transition as a free volume related kinetics phenomenon. *Acta Metall. Mater.* **38,** 383 (1990).